A study on the temporal and spatial variability of absorbing aerosols using Total Ozone Mapping Spectrometer and Ozone Monitoring Instrument Aerosol Index data

Jing Li,[1,2] Barbara E. Carlson,[2] and Andrew A. Lacis[2]

Received 16 October 2008; revised 23 January 2009; accepted 19 March 2009; published 9 May 2009.

[1] Absorbing aerosols, especially mineral dust and black carbon, play key roles in climate change by absorbing solar radiation, heating the atmosphere, and contributing to global warming. In this paper, we first examine the consistency of the Aerosol Index (AI) product as measured by the Total Ozone Mapping Spectrometer (TOMS) and Ozone Monitoring Instrument (OMI) instruments and then analyze these AI data sets to investigate the temporal and spatial variability of UV absorbing aerosols. In contrast to the trend in aerosol optical depth found in the advanced very high-resolution radiometer data, no obvious long-term trend in absorbing aerosols is observed from the time series of AI records. The comparison between the mean annual cycle in the two data sets shows that the cycles agree very well both globally and regionally, indicating a consistency between the AI products from TOMS and OMI. Varimax rotated Empirical Orthogonal Function (EOF) analysis of detrended, deseasonalized AI data proves to be successful in isolating major dust and biomass burning source regions, as well as dust transport. Finally, we find that large, individual events, such as the Kuwait oil fire and Australian smoke plum, are isolated in individual higher-order principal components.

Citation: Li, J., B. E. Carlson, and A. A. Lacis (2009), A study on the temporal and spatial variability of absorbing aerosols using Total Ozone Mapping Spectrometer and Ozone Monitoring Instrument Aerosol Index data, *J. Geophys. Res.*, *114*, D09213, doi:10.1029/2008JD011278.

1. Introduction

[2] Aerosols have been identified as the largest source of uncertainty in anthropogenic forcing of global climate change [*Charlson et al.*, 1992; *Hansen et al.*, 1997], because of the counteracting effects of absorbing and non-absorbing aerosols and because of their indirect effects on clouds. Absorbing aerosols affect the climate directly by altering radiation balance in the atmosphere [*Tegen et al.*, 1997; *Haywood and Boucher*, 2000; *Harrison et al.*, 2001; *Sokolik et al.*, 2001] and indirectly by affecting cloud nucleation and optical properties [*Levin et al.*, 1996; *Wurzler et al.*, 2000]. They also have the semidirect effect by heating the layer of the atmosphere and thus reducing cloud fraction [*Hansen et al.*, 1997]. Therefore it is necessary and important to investigate the global distribution and temporal variation of absorbing aerosols in the study of climate change. Two satellite instruments, Total Ozone Mapping Spectrometer (TOMS) and its heritage, Ozone Monitoring Instrument (OMI) both measure absorbing aerosols at UV wavelengths and their Aerosol Index (AI) product is well suited for this purpose. Version 8 AI is defined as

$$AI = -100\left[\log_{10}\left(I_{331}/I_{360}\right)_{meas} - \log_{10}\left(I_{331}/I_{360}\right)_{calc}\right] \quad (1)$$

where I_{meas} is the measured backscattered radiance at a given wavelength and I_{calc} is the backscattered radiance calculated at that wavelength for a pure Rayleigh atmosphere. Thus by this definition, AI is positive for UV absorbing aerosols, near zero for clouds and negative for scattering aerosols. However, because of ocean color variations and topographic features unresolved by the coarse resolution of the terrain database, negative AI values are largely contaminated by noise (O. Torres, personal communication, 2007). Therefore the current AI product only includes positive AI and is only useful for studying UV absorbing aerosols in a qualitative fashion. Quantitative products such as aerosol optical depth are also available for TOMS [*Torres et al.*, 2002] and OMI [*Torres et al.*, 2007].

[3] Among all types of UV absorbing aerosols, dust is the main contributor to the AI signal. Previously, several studies used the AI data set to identify dust sources. For example, *Prospero et al.* [2002], after specifying an AI threshold value of 1.0 for Northern Africa, concluded that the largest and most persistent sources are located in the Northern Hemisphere, mainly in a broad "dust belt" that extends from the west coast of North Africa, over the Middle East, Central and South Asia, to China. *Israelevich et al.* [2002]

[1]Department of Earth and Environmental Sciences, Columbia University, New York, New York, USA.
[2]NASA Goddard Institute for Space Studies, New York, New York, USA.

0148-0227/09/2008JD011278

inferred from long time average AI that Northern Africa is the most stable dust source in summer and that dust is transported eastward and northward along the Mediterranean basin. *Washington et al.* [2003] also used Nimbus 7 TOMS AI to identify dust-storm source areas. Their results revealed that in addition to Sahara, the Middle East, Taklimakan, South Asia, Central Australia, the Ethosha and Mkgadikgadi of Southern Africa, the Salar de Uyuni in Bolivia, and the Great Basin in the United States are also important dust-storm sources.

[4] In addition to dust, black carbon and some UV absorbing organic carbon aerosols also produce significant AI signals, especially with high concentration or altitude. *Habib et al*. [2006] found that TOMS AI bore a relation to anthropogenic aerosol emission strength in all regions of India except those with a strong mineral dust loading. *Badarinath et al.* [2007] also concluded that TOMS-OMI AI has good correlation in spatial patterns with fires. *Ji and Stocker* [2002] used Empirical Orthogonal Function (EOF) and Singular Spectrum Analysis (SSA) on TOMS data to study the global distribution and seasonal variation of fires. All of these studies suggest that biomass burning, which releases great amounts of black carbon and organic carbon into the atmosphere, contributes significantly to AI signals. Moreover, the AI is also sensitive to volcanic ash in the aftermath of volcanic eruptions [*Seftor et al.*, 1997]. However, none of the above studies focuses on or includes trend analysis of the AI record. Since *Massie et al.* [2004] observed an increase in Asian aerosols using TOMS Aerosol Optical Depth (AOD) data associated with weakly absorbing aerosols and *Mishchenko et al.* [2007a, 2007b] found temporal variations in the global mean advanced very high-resolution radiometer (AVHRR) aerosol optical depth, namely an increasing trend until 1991 and a decreasing trend thereafter, an additional motivation for this study is to examine the temporal variability, presence or absence of temporal trends, in UV absorbing aerosols over both land and ocean. It should be noted that while AVHRR is an ocean – only data set, the TOMS and OMI AI have observations over both land and ocean.

[5] In terms of time series analysis, one potential problem with the AI record is that the TOMS instrument has been successively placed on board several different satellites, first Nimbus 7 (N7), then Meteor 3 and Earth Probe (EP), and finally replaced with OMI on board Aura since 2005. Considering the disagreement between different aerosol products from satellite and ground observation found in previous intercomparison studies [*Mishchenko et al.*, 2007a, 2007b; *Liu et al.*, 2006], it is important to first examine the consistency of the whole AI record. No such studies on this purpose have been made previously. Therefore in this paper we first compared the mean annual cycle of N7 TOMS AI, EP TOMS AI and OMI AI. Because EP TOMS suffered from an instrumental degradation in 2000, we selected a 3 year period from 1997 to 1999 instead of the whole record. Meteor 3 TOMS AI is excluded from this study because of the unavailability of version 8 data. The reason to compare the mean annual cycle is that the three data sets have no overlap in time, making direct comparison impossible because of interannual variability in aerosol loading.

[6] Moreover, in order to link the temporal and spatial patterns in a large, multidimensional data set, the EOF method appears to be a useful tool, by separating the set into its constituent empirical orthogonal functions, or EOFs [*Peixoto and Oort*, 1992]. For example, *Washington et al.* [2003] used Varimax rotated EOF analysis of the annual TOMS AI anomalies for Sahara and identified Bodélé as the leading EOF, once the first unrotated EOF related to Saharan-wide dust had been removed. *Camp et al.* [2003] applied EOF analysis to detrended, deseasonalized TOMS ozone data to study total ozone variability in the tropics. In this particular study, we also use Varimax rotated EOF analysis on N7 TOMS, EP TOMS and OMI AI data over the spatial domain from 45°S to 45°N and 180°W to 180°E. It will be shown that this technique successfully isolates dust sources, dust transport, certain biomass burning sources and strong fire events.

2. Data Sources

[7] The TOMS AI data used in this study is version 8 N7 monthly mean and EP TOMS daily mean data sets, which are available from NASA GSFC FTP site (ftp://jwocky.gsfc.nasa.gov/pub/version8/aerosol). The data period for N7 TOMS is from January 1980 to December 1992 and January 1997 to December 1999 for EP TOMS, both with a 1.25° × 1.0° spatial resolution. Moreover, according to *Prospero et al.* [2002] and OMTO3 readme file (2008), only the AI values larger than +1 should be used for aerosol studies. Thus we set a threshold of +1 the two AI data sets. However, we also made test studies with smaller thresholds, and the results will be discussed in later sections. The EOF analysis of N7 AI data is mainly based on the monthly mean data. However, because EP TOMS AI has a much shorter record, we created a five-day mean data set from the daily data for EOF analysis.

[8] The OMI AI data is version OMTO3 daily data, also available from NASA GSFC FTP site (ftp://jwocky.gsfc.nasa.gov/pub/omi/data/aerosol). The data period is from January 2005 to December 2007 and the spatial resolution is 1.0° × 1.0°. Similar to Earth Probe TOMS, we also take five day mean from the daily data for the EOF analysis. The data has already been processed by the OMI team, with only AI values greater than +1 left.

3. Methodology: Rotated Empirical Orthogonal Function Analysis

[9] The object of EOF analysis is to decompose the data matrix into a set of independent, orthogonal eigenvectors, with the first eigenvector explaining the most of the variance, the second eigenvector explaining the most of the remaining variance, and so on. Assuming X is the data matrix of $M \times N$, where N is the number of locations (288 × 180 for TOMS and 360 × 180 for OMI) and M is the number of observations at each location. Then the EOFs are found by determining the eigenvectors of the covariance matrix C, which is

$$C = \frac{1}{M} XX^T \tag{2}$$

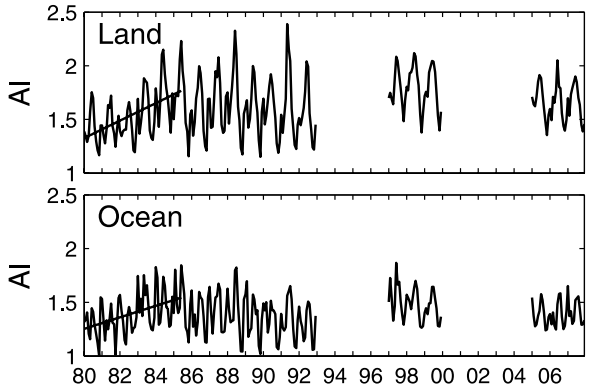

Figure 1. Time series of N7 TOMS AI, EP TOMS AI, and OMI AI combined. The solid line indicates trend fitted to the data from 1980 to 1985 and no trend shows afterward.

C is an $N \times N$ real, semidefinite matrix, and can therefore be written as

$$C = E\Lambda E^T \tag{3}$$

where Λ is a diagonal matrix whose elements are the N eigenvalues of C and E is an orthogonal matrix whose columns are the N orthogonal eigenvectors, i.e., EOFs. Each EOF has a corresponding time series, the so-called Principal Components (PCs), and the two satisfy

$$X = PE \tag{4}$$

where P is a $M \times N$ matrix whose columns are the N PCs.

[10] Combining equations (2), (3), and (4), we can see that

$$\Lambda = \frac{1}{M} P^T P \tag{5}$$

Since Λ is diagonal, the PCs are mutually orthogonal and the eigenvalues equal to their variances.

[11] However, the orthogonal constrain on EOFs sometimes causes the spatial structure of EOFs to have significant amplitudes all over the spectral domain and as a result, localized EOF structure cannot be obtained. In this case, it is usually necessary to apply rotated EOF analysis to relax the spatial orthogonal constrain, which means one seeks a $m \times m$ rotation matrix Q to construct the rotated EOFs U according to

$$U = EQ \tag{6}$$

here $E = [E_1, E_2, \ldots E_m]$ is the matrix of the leading m EOFs. In orthogonal rotations Q is chosen to be orthogonal.

$$QQ^T = I \tag{7}$$

[12] Varimax criterion is the most popular orthogonal rotation scheme because of the following criterion [*Kaiser*, 1958].

$$\max\left(\sum_{k=1}^{m}\left[\frac{1}{p}\sum_{j=1}^{p} u_{jk}^4 - \frac{1}{p^2}\left(\sum_{j=1}^{p} u_{jk}^2\right)^2\right]\right) \tag{8}$$

Where $U = (u_{ij})$ and m is the number of EOFs chosen for rotation (m = 24 in this study). In this criterion, the simplicity of the complete factor matrix is defined as the maximization of the sum of the simplicities of the individual factors.

[13] EOF analysis is not only able to isolate spatial and temporal structures of the data set, but can also be used to detect discontinuity or errors in the data.

4. Results and Discussion

4.1. Time Series of the Two Data Sets

[14] In the study of the temporal variability of UV – absorbing aerosols, we would like to examine if any trend exists in global as well as regional absorbing aerosol loading. The global mean time series for the three data sets are plotted together in Figure 1, with land and ocean separated. However, unlike the continuous trend obtained from AVHRR aerosol optical depth, there is an increase in AI from 1982 to1985 and essentially no trend afterwards. A similar pattern is found in West Sahara, Sahel, North Atlantic and Australia but no trend is seen in other major absorbing aerosol source regions (figure not shown). The trend pattern for the West Sahara and Sahel agrees with the Barbados dust record [*Prospero*, 1999; *Chiapello et al.*, 2005] and the results of the study by *Anuforom et al.* [2007]. At present, trend analysis using the AI data is complicated by a number of factors. While AVHRR optical depths are independent of aerosol type and height and depend solely on the aerosol concentration the AI data depend on aerosol type (strength and spectral dependence of aerosol UV absorption) and height of the aerosol layer (strength of the spectrally dependent molecular Rayleigh scattering contribution). An additional complication is the nature of and persistence of the aerosol. The lack of a clear long-term trend in AI data is probably because most of its signal comes from short-term events such as wind blown dust or biomass burning, and the sources are mostly natural such as the Sahara desert, and there is hardly any trend in these individual events. This is probably also why no ENSO pattern shows in the time series because the events are too short to be strongly influenced by ENSO. While for AVHRR, sea salt, sulfate and nitrate aerosols contribute a large portion to its optical depth measurement, and these are persistent signals and many of them are anthropogenic. Nevertheless, because of the problems in the Meteor 3 TOMS and EP TOMS AI, absorbing aerosol trend information for the periods 1992 to 1996 and 2000 to 2004 is not available, making it impossible to perform a more direct comparison with the AVHRR optical depth trend at this time. The lack of an obvious trend in the AI data does not mean that there is not a trend in one of the types of UV-absorbing aerosol, because the AI data involves the interaction among all absorbing aerosols in the atmosphere, is sensitive to aerosol height and the results of our analysis are sensitive to the value of the AI threshold used in the analysis. It is possible that trends exist for certain types of absorbing aerosols. For example, *Massie et al.* [2004] discovered an increasing trend in India and China aerosols mostly associated with weakly – absorbing sulfate aerosols from TOMS AOD data. *Habib et al.* [2006] also found an increase in black carbon and inorganic matter emissions over India from 1981 to 1999. Therefore more accurate

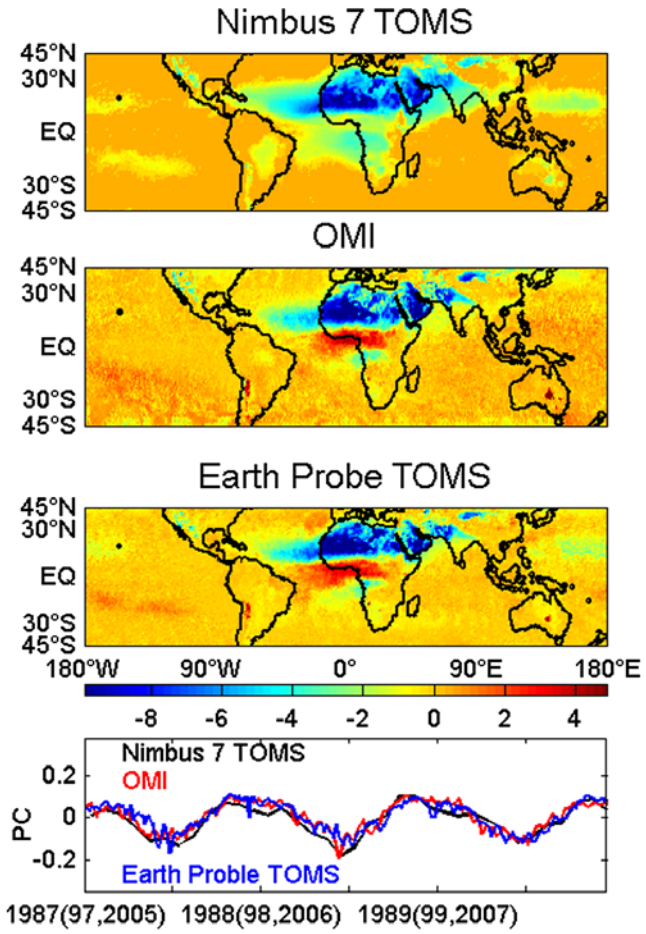

Figure 2. The first EOF of the three data sets and their PCs over the three-year period (1987–1989 for N7 TOMS, 1997–1999 for EP TOMS, and 2005–2007 for OMI). The EOF together with its PC indicates that the global mean pattern of the three data sets is consistent.

trend analysis on absorbing aerosols requires the combination of other measurements, such as ground observation.

4.2. Mean Annual Cycle Comparison

[15] The mean annual cycle of the three data sets is compared both globally and regionally. First of all, EOF analysis is carried out on the original monthly mean N7 TOMS AI, five-day mean EP TOMS AI and five-day mean OMI AI data sets. In this way, the first EOF, together with its PC, show the mean status (Figure 2). It is clearly seen that the three EOFs are identical, with major feature of the main dust belt extending from West Sahara to Central Asia. Australian dust, dust transport off West African coast and dust combined with biomass burning over Sahel and South Africa can also be identified. The three PCs over the three-year period are plotted on Figure 2 (bottom). For N7 TOMS the time period is from 1987 to 1989, for EP TOMS it is from 1997 to 1999 and for OMI it is from 2005 to 2007. The three PCs also agree well in terms of the three-year annual cycle, which indicate that the mean status of N7 TOMS, EP TOMS and OMI data sets are consistent globally.

[16] Furthermore, in order to make localized comparisons, we selected 12 key geographic locations according to the results of EOF analysis in the next section (Figure 3). These regions represent the major absorbing aerosol regimes, e.g., dust from Sahara, Persian Gulf and off the west coast of Africa; dust in Taklimakan; dust in Australia; biomass burning of South Africa and South America and biomass burning combined with southward dust flow in Sahel. The mean annual cycles are obtained by averaging the AI data over each month or each five-day period for these areas. From this comparison it is found that the EP TOMS and OMI mean annual cycles agree well with the N7 TOMS mean annual cycle, i.e., the variation is found to be within ± the standard deviation of the N7 TOMS AI cycle (Figure 4).

[17] The global and regional comparisons between mean annual cycles of the three data sets clearly indicate that the three AI data sets are consistent. Although the three data sets are supposed to be the same product with the same algorithm, considering they are different instruments, or on different satellites, and previous disagreement between MODIS TERRA and MODIS AQUA [*Mishchenko et al.*, 2007a, 2007b], this result is meaningful for future studies on UV absorbing aerosols.

4.3. Rotated Empirical Orthogonal Function Analysis

[18] In this section, we present results from Varimax rotated EOF analysis of detrended and deseasonalized

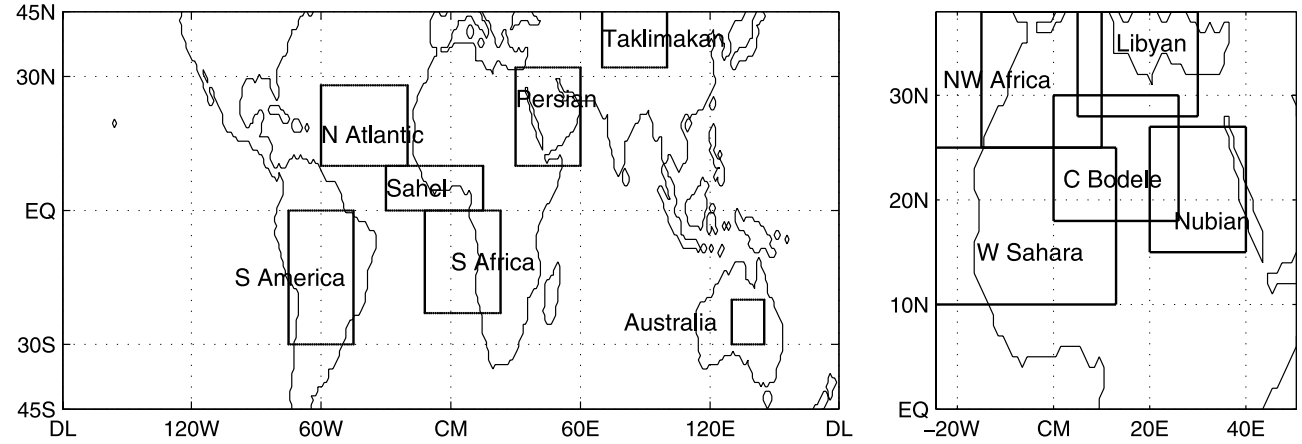

Figure 3. Regions selected according for the EOF analysis for mean annual cycle comparison.

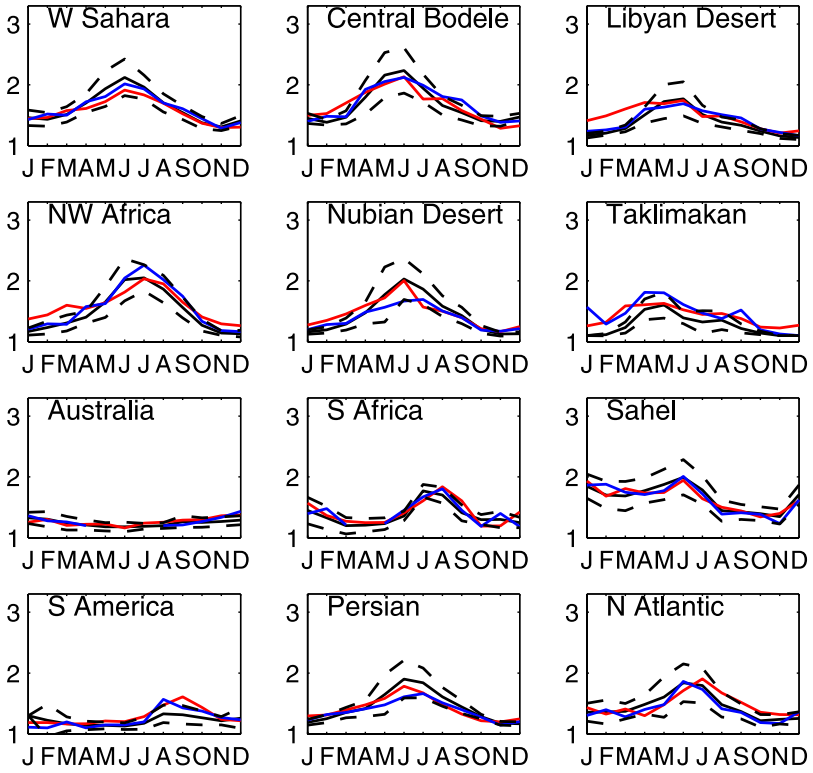

Figure 4. Mean annual cycle of N7 TOMS, EP TOMS, and OMI monthly mean data over the 12 selected regions. (black) N 7 TOMS; (blue) EP TOMS; (red) OMI; (black dashed) ±standard deviation of N7 monthly mean TOMS AI. The mean annual cycles of EP TOMS and OMI AI generally vary within the ±standard deviation of N7 AI data, meaning that the three data sets are consistent regionally.

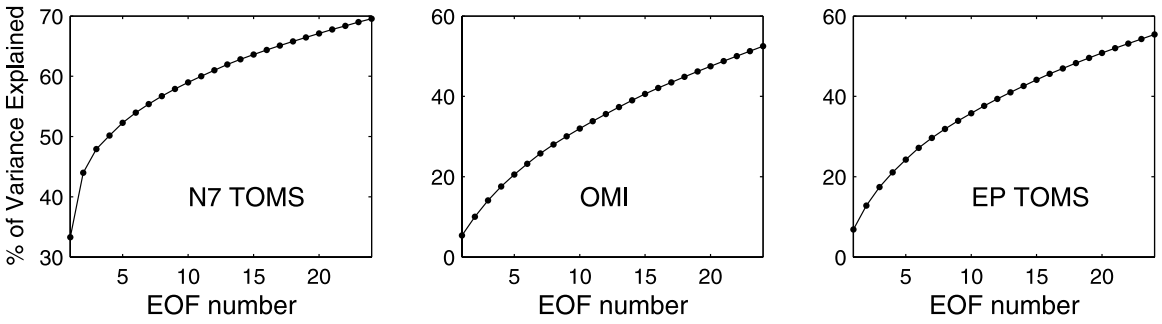

Figure 5. Percentage of variance explained by the first 24 REOFs of the three data sets. The curve for N7 TOMS data resembles that of most other EOF analysis, with the dominant EOF explaining much greater variance, whereas for EP TOMS and OMI data, the variance explained is more evenly distributed among the REOFs.

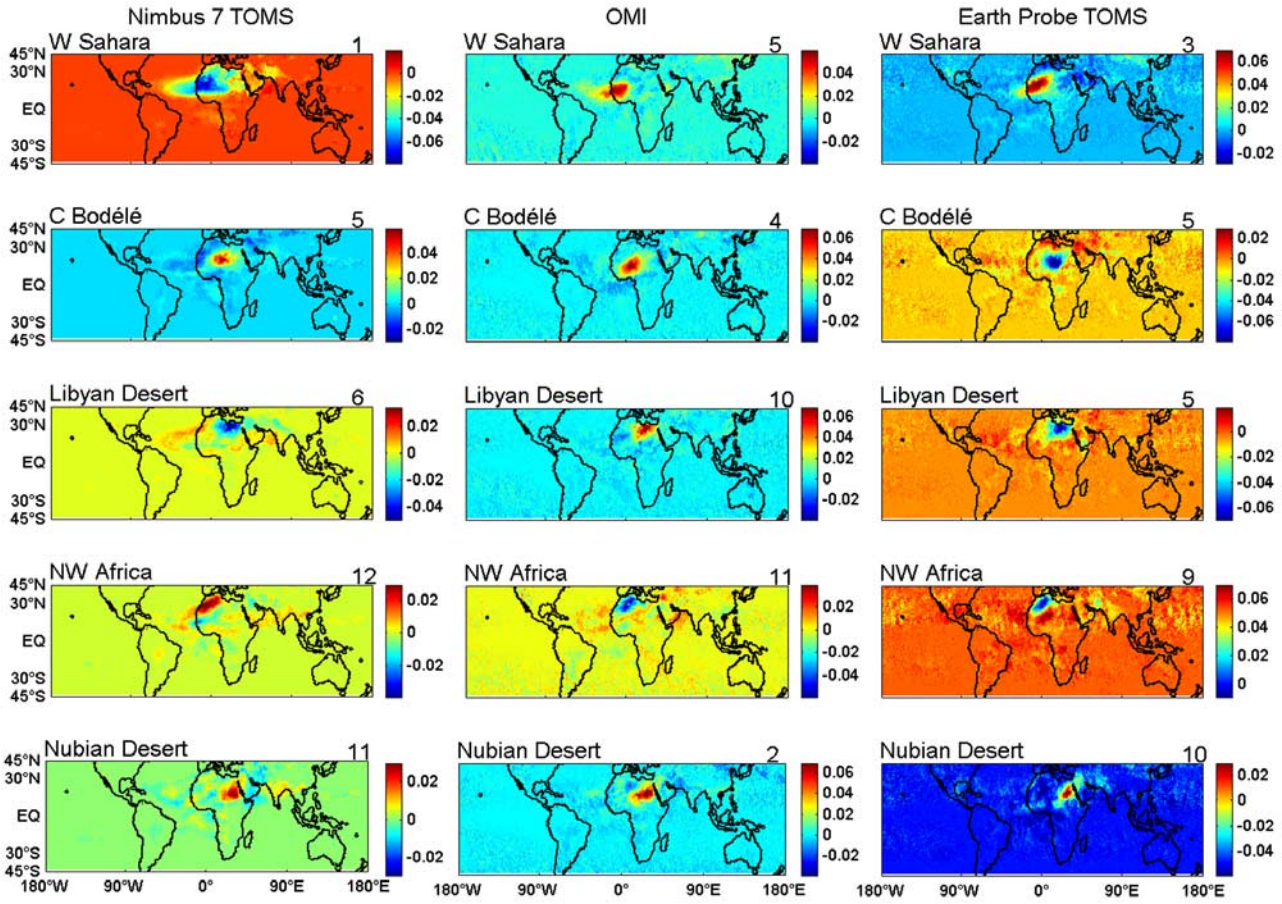

Figure 6. Major dust sources in North Africa: West Sahara, Central Bodélé depression, Libyan desert, Northwest Africa, and Nubian Desert are shown in the REOFs of N7 TOMS, EP TOMS, and OMI AI data. The number on the right corner indicates the order of the EOF. The result supports previous works but indicates West Sahara as the most important dust source over both Africa and the globe.

TOMS and OMI AI data sets to further examine the temporal and spatial variability of absorbing aerosols. Varimax rotated EOF analysis is effective in isolating local patterns but might not be able to identify global modes [*Dommenget and Latif*, 2001]. Because most of the UV absorbing aerosols arise from local sources, this method appears to be suitable.

[19] Unlike the results of EOF analyses of other climatic variables e.g., clouds, precipitation where the dominant mode of interannual variability is linked to ENSO, the AI EOF patterns clearly show major dust and biomass burning sources and strong individual events. The PCs are largely related to the AI time variation of the source region. Unlike most EOF analysis studies, the leading EOFs of N7 TOMS AI data account for only a small portion of the total variance explained, and even less for EP TOMS and OMI AI data. Here we present the first 24 Rotated EOFs (REOFs) for the three data sets. Although the total variances explained by them are 69.6%, 55.4% and 52.5%, respectively (Figure 5), their spatial patterns have essentially included most of the information. The difference between the shape of the curves between the monthly mean data set and the two five-day mean data sets is mostly likely caused by the short record of EP TOMS and OMI AI.

[20] Major dust sources in North Africa are shown individually in the first few REOFs, for both data sets (Figure 6). The dust sources can be identified as (1) Western Sahara, covering east of Mauritania coast and Mali; (2) Central Bodélé depression in Chad; (3) the Libyan Desert; (4) Northwest Africa, covering North Algeria; and (5) the Nubian desert, covering Sudan and South Egypt. These dust sources are in excellent agreement with *Washington et al.* [2003] and *Engelstaedter et al.* [2006]. The only disagreement is that both of these studies identify the Bodélé depression as the most important source, but in our study, Western Sahara appears as the dominant REOF. Considering that we use a more comprehensive data set than previous studies, this suggests that Western Sahara is the dominant dust source over the globe. For OMI data, the order of the OMI REOFs corresponding to the five source regions differs from that in the TOMS data. While the mean annual cycles agree, they have different time variability around the mean because of temporal changes in dust events. In addition to the five major North African dust sources, other weaker dust sources can also be identified, such as Taklimakan desert and Australian dust (Figure 7). The Australian pattern is absent in the EP TOMS REOFs. We note however, that the information for this region is spread over several REOFs,

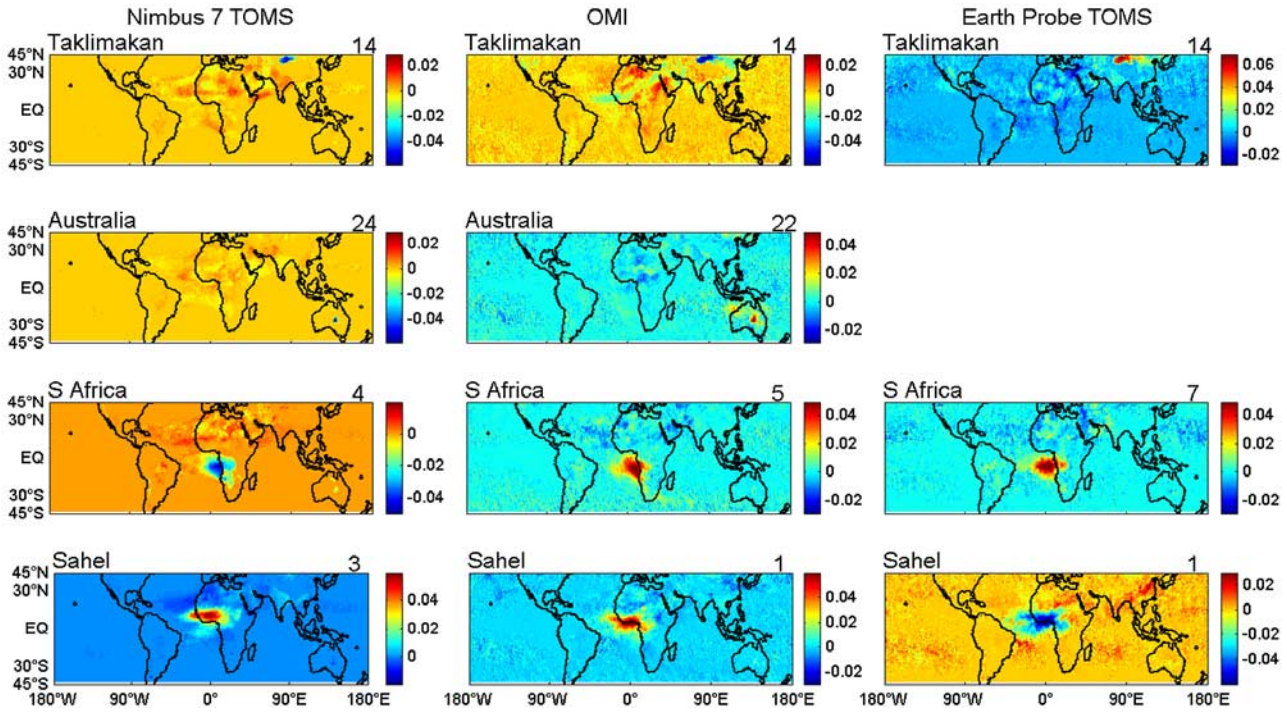

Figure 7. REOFs of N7 TOMS, EP TOMS, and OMI show Taklimakan, Australia, South Africa, and Sahel. The Australia pattern is distributed in several REOFs in the EP TOMS AI data set instead of being isolated in a single one. Similarly, the southern part of the Sahel region appears in another REOF for the N7 TOMS data set. Therefore the pattern of the third REOF is further north compared with EP TOMS and OMI AI data.

instead of being isolated in a single REOF as the N7 TOMS and OMI results, probably because this signal is not strong or persistent enough compared with that in the other two data sets.

[21] Moreover, biomass burning in South Africa and biomass burning combined with dust transport over the Sahel are also clearly indicated in two separate REOFs, for both data sets (Figure 7). The Sahel region shown in the N7 TOMS data set is further north compared with the other two, because the Sahel is separated into two REOFs for this data set, with the seventh REOF showing the southern part of this region (figure not shown). The cause of this phenomenon might be mainly caused by the different time periods of the data sets.

[22] As mentioned in section 2, we specified an AI threshold of +1 for the TOMS data set. This successfully reduces noise over the ocean and cloud contamination but may also eliminate some of the aerosol signal. For example, biomass burning in South America produces a comparatively weaker AI signal (AI values less than +1 in winter). Testing the sensitivity of our results to the value of the AI threshold we find that a coherent feature associated with biomass burning is isolated in the twenty first REOF for an AI threshold of 0.3. The importance of this source increases when no threshold is used. It is isolated in the seventh REOF with no AI threshold. Moreover its PC agrees very well with the time series for this region (Figure 8). For the OMI data set, since all of the AI values are greater than one, this feature (EOF) is missing. This raises questions of how best to analyze the AI data and whether or not it is appropriate to simply set an AI threshold considering the complicated AI dependence in aerosol type and height distribution.

[23] Rotated EOF analysis is also able to identify strong, individual events. For example, the second N7 TOMS REOF and its PC show the famous Kuwait oil fire in 1991. The PC corresponds well with the time series of the Kuwait region, with a strong peak in 1991 (Figure 9, left). It is also worth noting that the Persian Gulf region is also a

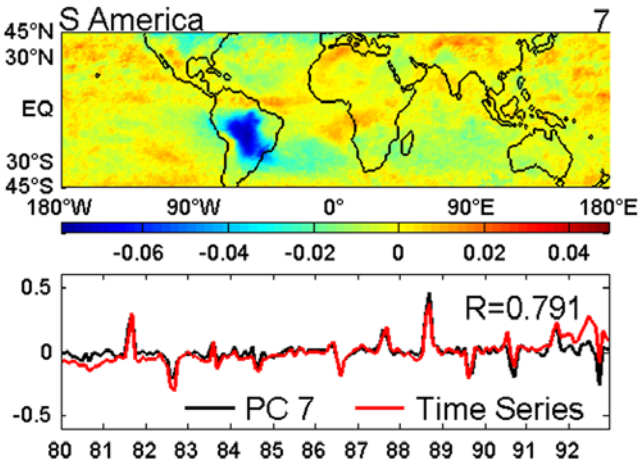

Figure 8. After including AI < 1, the seventh REOF of N7 TOMS data shows biomass burning over South America. The correlation coefficient between PC 7 and the time series of this region is very high (R = 0.791).

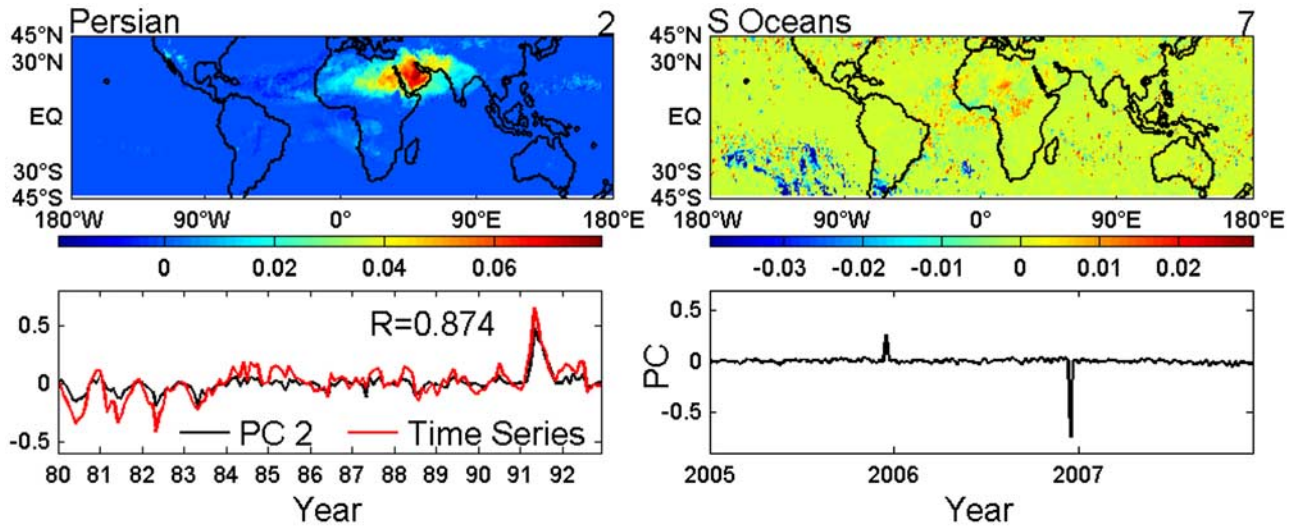

Figure 9. (left) The second REOF of N7 TOMS AI data shows the great Kuwait oil fire in June 1991. The PC again has high correlation with the time series of the Persian Gulf region (R = 0.874) with a strong peak in 1991. (right) The seventh REOF of the OMI AI data set shows a smoke plume over the South Oceans in December 2006 from Australian brush fires.

dust source, so this region appears in the ninth EOF of OMI data when there were no strong fires. The seventh REOF and its PC of the OMI AI data set correspond to a strong smoke plume triggered by brush fires in Australia and traveled over the South Oceans in December 2006 (Figure 9, right) [*Torres et al.*, 2007]. The small peak in the PC series in December 2005 is very likely an artifact of the EOF analysis, as no significant feature is observed in the AI map during that period.

[24] Our REOFs also provide information on the transport of dust from source regions. For example, the eighth OMI REOF, plotted in Figure 10 (top) is suggestive of transport from the source shown in the second OMI REOF (Figure 6). Supporting this interpretation is the correlation between PC 8 and PC 2 which is found to be higher at lag −15 (Figure 10, bottom). Moreover, this result agrees with the trajectories of the dust transport indicated by *Engelstaedter et al.* [2006]. Similar patterns are also seen in the N7 TOMS and EP TOMS REOFs suggesting that REOF analysis is useful for transport studies.

5. Conclusion

[25] Motivated by the disagreements between various satellite aerosol products and the recently revealed aerosol trend, we carried out this study to examine the consistency of the TOMS and OMI AI records and to investigate the spatial and temporal variability of UV absorbing aerosols. In contrast to the continuous trend in AVHRR aerosol optical thickness data, except for an increase in AI from 1982 to 1985, there is no long-term trend in the AI record. The most important conclusion is that monthly mean EP TOMS AI and OMI AI annual cycles agree very well with monthly mean N7 TOMS AI both globally and regionally, indicating that the AI product is a consistent absorbing aerosol record. This result provides a basis for combined studies using both TOMS and OMI data in the future. Moreover, Varimax rotated EOF analysis of the two data sets reveals useful spatial and temporal information identifying source regions and dust trajectories as well as providing quantitative information on the relative strengths of the sources. Strong, individual events, such the Kuwait oil fire and a strong Australia smoke plume, are captured in individual, high order, REOFs. Furthermore, dust transport over the North Atlantic Ocean is also separated in an individual EOF in the OMI data set.

[26] The results of our EOF analysis of AI data show that this technique is useful to objectively identify aerosol sources, study aerosol transport trajectories and isolated aerosol events. It also supports regional comparison studies

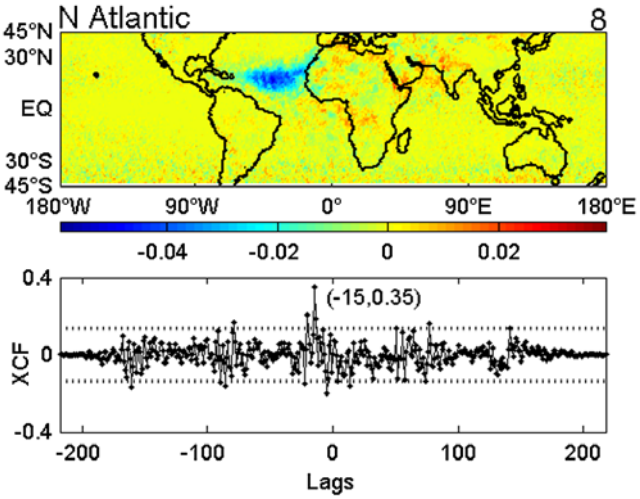

Figure 10. Dust transport over North Atlantic Ocean appears in the eighth REOF of OMI AI data. The bottom is the cross correlation between PC 8 and PC 2; the two dotted lines indicate the 95% confidence interval and that the two series are uncorrelated. It can be seen that there is a peak at lag −15 (75 days) in the cross-correlation function.

by objectively confirming the relevant spatial domain. Nonetheless, our results indicate that because of the qualitative nature of the AI product and its dependence on aerosol type and height further investigation using correlative measurements is required to completely address temporal trends in the AI product.

[27] **Acknowledgments.** We thank the TOMS and OMI science team for providing the AI data used in this study. We also thank Omar Torres for providing useful information regarding the AI data.

References

Anuforom, A. C., L. E. Akeh, P. N. Okeke, and F. E. Opara (2007), Interannual variability and long term trend of UV-absorbing aerosols during Harmattan season in sub-Saharan West Africa, *Atmos. Environ.*, *41*, 1550–1559.

Badarinath, K. V. S., S. K. Kharol, and T. R. K. Chand (2007), Use of satellite data to study the impact of forest fires over the northeast region of India, *IEEE Trans. Geosci. Remote Sens.*, *4*, 485–489.

Camp, D. C., M. S. Roulston, and Y. J. Yung (2003), Temporal and spatial patterns of the interannual variability of total ozone in the tropics, *J. Geophys. Res.*, *108*(D20), 4643, doi:10.1029/2001JD001504.

Charlson, R. J., S. E. Schwartz, J. M. Hales, R. D. Cess, J. A. Coakley Jr., J. E. Hansen, and D. J. Hoffman (1992), Climate forcing by anthropogenic aerosols, *Sciences*, *255*, 423–430.

Chiapello, I., C. Moulin, and J. M. Prospero (2005), Understanding the long-term variability of African dust transport across the Atlantic as recorded in both Barbados surface concentrations and large-scale Total Ozone Mapping Spectrometer (TOMS) optical thickness, *J. Geophys. Res.*, *110*, D18S10, doi:10.1029/2004JD005132.

Dommenget, D., and M. Latif (2001), A cautionary note on the interpretation of EOFs, *J. Clim.*, *15*, 216–225.

Engelstaedter, S., I. Tegen, and R. Washington (2006), North African dust emissions and transport, *Earth Sci. Rev.*, *79*, 73–100.

Habib, G., C. Venkataraman, I. Chiapello, S. Ramachandran, O. Boucher, and M. S. Reddy (2006), Seasonal and interannual variability in absorbing aerosols over India derived from TOMS: Relationship to regional meteorology and emissions, *Atmos. Environ.*, *40*, 1909–1921.

Hansen, J., M. Sato, and R. Reudy (1997), Radiative forcing and climate response, *J. Geophys. Res.*, *102*, 6831–6864.

Harrison, S. P., K. E. Kohfeld, C. Roelandt, and T. Claquin (2001), The role of dust in climate changes today, at the Last Glacial Maximum and in the future, *Earth Sci. Rev.*, *54*, 43–80.

Haywood, J., and O. Boucher (2000), Estimates of direct and indirect radiative forcing due to tropospheric aerosols, *Rev. Geophys.*, *38*, 513–543.

Israelevich, P. L., Z. Levin, J. H. Joseph, and E. Ganor (2002), Desert aerosol transport in the Mediterranean region as inferred from the TOMSO Aerosol Index, *J. Geophys. Res.*, *107*(D21), 4572, doi:10.1029/2001JD002011.

Ji, Y., and E. Stocker (2002), Seasonal, intraseasonal, and interannual variability of global land fires and their effects on atmospheric aerosol distribution, *J. Geophys. Res.*, *107*(D23), 4697, doi:10.1029/2002JD002331.

Kaiser, H. F. (1958), The varimax criterion for analytic rotation in factor analysis, *Psychometrika*, *23*, 187–200.

Levin, Z., E. Ganor, and V. Gladstein (1996), The effects of desert particles coated with sulfate on rain formation in the eastern Mediterranean, *J. Appl. Meteorol.*, *35*, 1511–1523.

Liu, L., A. A. Lacis, B. E. Carlson, M. I. Mishchenko, and B. Cairns (2006), Assessing Goddard Institute for Space Studies ModelE aerosol climatology using satellite and ground-based measurements: A comparison study, *J. Geophys. Res.*, *111*, D20212, doi:10.1029/2006JD007334.

Massie, S. T., O. Torres, and S. T. Smith (2004), Total Ozone Mapping Spectrometer (TOMS) observation of increases in Asian aerosol in winter from 1979 to 2000, *J. Geophys. Res.*, *109*, D18211, doi:10.1029/2004JD004620.

Mishchenko, M. I., I. V. Geogdzhayev, B. Cairns, B. E. Carlson, J. Chowdhary, A. A. Lacis, L. Liu, W. B. Rossow, and L. D. Travis (2007a), Past, present, and future of global aerosol climatologies derived from satellite observations: A perspective, *J. Quant. Spectrosc. Radiat. Transfer*, *106*, 325–347.

Mishchenko, M. I., I. V. Geogdzhayev, W. B. Rossow, B. Cairns, B. E. Carlson, A. A. Lacis, L. Liu, and L. D. Travis (2007b), Long-term satellite record reveals likely recent aerosol trend, *Science*, *315*(5818), 1543, doi:10.1126/science.1136709.

Peixoto, J. P., and A. H. Oort (1992), *Physics of Climate*, American Institute of Physics, College Park, Md.

Prospero, J. M. (1999), Long-term measurements of the transport of African mineral dust to the southeastern United States: Implications for regional air quality, *J. Geophys. Res.*, *104*, 15,917–15,927.

Prospero, J. M., P. Ginoux, O. Torres, S. E. Nicholson, and T. E. Gill (2002), Environmental characterization of global sources of atmospheric soil dust identified with the nimbus7 total ozone mapping spectrometer (TOMS) absorbing aerosol product, *Rev. Geophys.*, *40*(1), 1002, doi:10.1029/2000RG000095.

Seftor, C. J., N. C. Hsu, J. R. Herman, P. K. Bhartia, O. Torres, W. I. Rose, D. J. Schneider, and N. Krotkov (1997), Detection of volcanic ash clouds from Nimbus 7/total ozone mapping spectrometer, *J. Geophys. Res.*, *102*, 16,749–16,759.

Sokolik, I. N., D. M. Winker, G. Bergametti, D. A. Gillette, G. Carmichael, Y. Kaufman, L. Gomes, L. Schuetz, and J. E. Penner (2001), Introduction to special section: Outstanding problems in quantifying the radiative impacts of mineral dust, *J. Geophys. Res.*, *106*, 18,015–18,028.

Tegen, I., P. Hollrig, M. Chin, I. Fung, D. Jacob, and J. Penner (1997), Contribution of different aerosol species to the global aerosol extinction optical thickness: Estimates from model results, *J. Geophys. Res.*, *102*, 23,859–23,915.

Torres, O., P. K. Bhartia, J. R. Herman, A. Sinyuk, P. Ginoux, and B. Holden (2002), A long-term record of aerosol optical depth from TOMS observations and comparison to AERONET measurements, *J. Atmos. Sci.*, *59*(3), 398–413.

Torres, O., A. Tanskanen, B. Veihelmann, C. Ahn, R. Braak, P. K. Bhartia, P. Veefkind, and P. Levelt (2007), Aerosols and surface UV products from Ozone Monitoring Instrument observations: An overview, *J. Geophys. Res.*, *112*, D24S47, doi:10.1029/2007JD008809.

Washington, R., M. Todd, N. J. Middleton, and A. S. Goudie (2003), Dust-storm source areas determined by the total ozone monitoring spectrometer and surface observations, *Ann. Assoc. Am. Geogr.*, *93*(2), 297–313.

Wurzler, S., T. G. Reisin, and Z. Levin (2000), Modification of mineral dust particles by cloud processing and subsequent effects on drop size distributions, *J. Geophys. Res.*, *105*, 4501–4512.

B. E. Carlson, NASA Goddard Institute for Space Studies, 2880 Broadway, Room 646, New York, NY 10025, USA.

A. A. Lacis, NASA Goddard Institute for Space Studies, 2880 Broadway, Room 658, New York, NY 10025, USA.

J. Li, Department of Earth and Environmental Sciences, Columbia University, 2880 Broadway, Room 536, New York, NY 10025, USA. (jli@giss.nasa.gov)